Science
AAAS

Supplementary Materials for

Steps toward translocation-independent RNA polymerase inactivation by terminator ATPase ρ

Nelly Said, Tarek Hilal, Nicholas D. Sunday, Ajay Khatri, Jörg Bürger, Thorsten Mielke, Georgiy A. Belogurov, Bernhard Loll, Ranjan Sen, Irina Artsimovitch, Markus C. Wahl

Correspondence to: artsimovitch.1@osu.edu; markus.wahl@fu-berlin.de

This PDF file includes:

- Materials and Methods
- Figs. S1 to S12
- Tables S1 to S5
- Captions for Movies S1 to S2

Other Supplementary Materials for this manuscript include the following:

- Movies S1 to S2

Materials and Methods

Protein production for transcription assays

Plasmids used for protein production are listed in Table S4. For transcription assays, WT RNAP and variants were purified as described previously (*55*), following expression in XJb (DE3) strain (Zymo Research). For purification of Δω RNAP, a Δ*rpoZ* XJb strain was constructed by P1-mediated transduction of the *rpoZ*::kan allele from a Keio knockout collection (*56*).

For production of NusG$^{\Delta HL}$, XJB cells were transformed with pMT037, grown to OD_{600}=0.4 and induced with 0.5 mM IPTG for 3 hours at 37 °C. Cells were resuspended in LysT buffer (50 mM Tris-Cl, 500 mM NaCl, 5 %[v/v] glycerol, 20 µM PMSF, pH 6.9) supplemented with 1X EDTA-free Complete Protease Inhibitors cocktail (Roche), disrupted *via* sonication and cleared *via* centrifugation. The cleared extract was applied to a 1 ml HisTrap HP column (GE Healthcare) and eluted with a shallow gradient with LysT buffer supplemented with 1 M imidazole. Fractions containing NusG$^{\Delta HL}$ were pooled and applied to a Superdex 75 gel filtration column (GE Healthcare) equilibrated with 2X storage buffer (0.02 M Tris-Cl, 5 % [v/v] glycerol, 0.02 mM EDTA, 0.2 M NaCl, 0.2 mM DTT, pH 7.9). Fractions containing NusG$^{\Delta HL}$ were pooled and mixed 1:1 with 100 % glycerol.

Production of ρ-EC for cryoEM analysis

Protein components of ρ-ECs and variants thereof were produced and purified as described before (*24, 57*). RNA containing the λ tR1 *rut* region was produced by *in vitro* transcription and purified as described before (*57*). Scaffold DNA oligomers were purchased from Eurofins.

For ρ-EC formation, equimolar amounts of template DNA and *rut* RNA were mixed in 10 mM Tris-Cl, 40 mM KCl, 5 mM $MgCl_2$, pH 8.0, heated to 95 °C for 5 min and subsequently cooled to 25 °C at 1 °C/min (Fig. S2B). The annealing product was incubated in running buffer

(20 mM Tris-Cl, 120 mM KOAc, 5 mM $Mg(OAc)_2$, 10 μM $ZnCl_2$, 2 mM DTT, pH 8.0) with RNAP in a 1.3:1 molar ratio on ice for 10 min, then at 32 °C for 10 min. An equimolar amount of non-template DNA was added and incubated for another 5 min. Afterwards, a threefold molar excess of NusA and NusG was added, followed by incubation at 32 °C for 15 min. The mixture was chromatographed on a Superdex 200 Increase 3.2/300 gel filtration column (GE Healthcare) in running buffer, and fractions containing NusA/NusG-EC were pooled. NusA/NusG-EC was mixed with a threefold molar excess of ρ hexamer, and the mixture was incubated at 32 °C for 15 min. 1 mM ADP-BeF_3 was then added to the sample, followed by incubation at 18 °C for 5 min.

Single-particle cryoEM data collection, processing and structural analysis

Freshly prepared ρ-ECs (5 mg/ml) were supplemented with n-octylglucoside to a final concentration of 0.15 % (w/v) immediately before grid preparation to overcome preferred particle orientation. 3.8 μl of the sample were applied to plasma-treated Quantifoil R1/4 holey carbon grids, blotted and plunged into liquid ethane using an FEI Vitrobot Mark IV at 10 °C/100 % humidity. Data were acquired on a 300 kV FEI Tecnai G^2 Polara cryo-transmission electron microscope, equipped with a Gatan K2 Summit direct electron detector in super-resolution mode, with a pixel size of 0.62 Å on the object scale. A total electron dose of 50 $e^-/Å^2$ was accumulated during a 10 s exposure. During four independent imaging sessions, a total of 9887 movies were acquired automatically using Leginon (*58*).

Dose-weighted, aligned micrographs were calculated with MotionCor2 (*59*), ctf estimation was done with Gctf (*60*). Data analysis was done within the cryoSPARC2 framework (*61*). Manually picked particle images were used to generate an initial template for reference-based particle picking (2,112,813 particle images). Particle images were extracted with a box size of 600 px and binned to 100 px, yielding a pixel-size of 3.72 Å/px. 2D classification was applied to remove obviously false-positive picks. A small subset of particles belonging to the best class averages were used for an *ab initio* reconstruction, which was further used as starting reference for iterative, heterogeneous 3D classification (*21*). A final dataset of 389,380 particle images representing ρ-ECs was re-extracted with a box of 300 px and homogeneously refined to 3.75 Å resolution. Particle coordinates and refinement parameters were exported using pyem (*62*) and used for extraction of particles with RELION (*63*), binned to a box size of 100 px. 3D classification was conducted with cisTEM (*64*) to isolate the nine complexes described here by a combination of global and focused classifications. Particle orientation parameters were not refined during the entire hierarchical classification procedure. Particle images belonging to each complex were individually subjected to non-uniform refinement in cryoSPARC2 at a box size of 300 px to yield the final reconstructions.

Model building and refinement

Coordinates for ρ-EC components from previously determined sub-structures were docked into the cryoEM maps using Coot (*65*). Proteins and nucleic acids were manually rebuilt into the cryoEM densities. Structural models were manually adjusted residue-by-residue, supported by real space refinement in Coot. The manually built models were refined against the cryoEM maps using the real space refinement protocol in PHENIX (*66*). To avoid overfitting, the weighting factor between model geometry and data applied during real-space refinement was optimized by refining the model against one half-set of the data and comparing cross-resolutions between the refined model with this half-set (FSC_{work}) and the unused half-set (FSC_{test}). Deviations in FSC_{work} and FSC_{test} curves indicate overfitting and should be minimal. A weighting factor of 1 was determined to be optimal (Fig. S6) and used for final refinement of the model into the map of the full dataset. Structure figures were prepared using PyMOL (Version 1.8 Schrödinger, LLC).

Structure comparisons

Structures were compared and RMSD values were calculated by global superposition of complex structures or by superposition of selected subunits in complexes using the “secondary structure matching” algorithm implemented in Coot or the “align” algorithm implemented in PyMOL.

Transcription assays

RNAP holoenzymes were assembled by mixing core RNAP (wild-type or mutationally altered) with a threefold molar excess of σ^{70} transcription initiation factor, followed by incubation at 30 ºC for 20 min. Phage λ tR1 DNA template was generated by PCR amplification and purified by PCR cleanup kit (QIAGEN). Halted A26 ECs were formed at 37 ºC for 12 min by mixing 40 nM RNAP holoenzyme with 20 nM λ tR1 DNA template, 100 µM ApU, 10 µM ATP and UTP, 2 µM GTP, and 5 Ci/mmol [α^{32}P]-GTP in ρ termination buffer (40 mM Tris-Cl, 50 mM KCl, 5 mM $MgCl_2$, 0.1 mM DTT, 3 % (v/v) glycerol, pH 7.9). ρ, NusA, and NusG were added to 20, 100, or 300 nM, respectively, and the reactions incubated for an additional 3 min at 37 ºC. While NusA, NusG, and WT RNAP activities remain constant over extended (10 years) storage at -20 ºC, the ρ activity declines more noticeably (~20% after 2 years). Since this may result in experimental variability, we perform each assay with the WT RNAP as a control. In assays with RNAP mutants shown here, the termination efficiency for the WT RNAP remained constant: 82.8 ± 2.2% (n=12). However, in experiments with “old” ρ in Fig. 2B, termination was reduced. Thus, if absolute ρ activity is important, single-use aliquots should be used. In Fig. S1A, GreA, RapA, and Mfd were added at 1 µM; GreB – at 200 nM. Transcription was restarted by addition of a pre-warmed (37 ºC) mixture containing all four NTPs and rifapentin to a final concentration of 200 µM and 50 µg/ml, respectively (except for Fig. 7D, where NTPs were titrated), and incubated at 37 ºC for 6 min. Reactions were quenched by addition of an equal volume of stop buffer (45 mM Tris-borate, 10 M urea, 20 mM EDTA, 0.2 % xylene cyanol, 0.2 % bromophenol blue, pH 8.3) and separated by denaturing 5 % PAGE (7 M urea, 0.5X TBE). Gels were dried and products were visualized using a Typhoon FLA 9000 PhosphorImaging system (GE Healthcare Life Sciences). Readthrough and termination RNA products were quantified with ImageQuant and Microsoft Excel software.

Analytical size exclusion chromatography

For interaction tests between RNAP, NusA and ρ, proteins were mixed in running buffer (20 µM final concentration) and incubated at 32 °C for 15 min. For testing ρ interaction with EC harboring *rut* RNA, EC was assembled and purified as described for cryoEM and incubated with ρ at 32 °C for 15 min. Mixtures were chromatographed on a Superose 6 Increase 3.2/300 column (GE Healthcare) with a flow rate of 40 µl/min, and 50 µl fractions were collected. Fractions were analyzed by 15 % SDS-PAGE gels and urea-PAGE.

Genetic screens, growth analysis and *in vivo* termination assays

Bacterial strains, plasmids and phages are listed in Table S5. All growth and *in vivo* transcription termination assays were done with *E. coli* MC4100 (RS1428) and derivatives. RS1428 produces ρ^{WT} and contains a P_{RM}-*racR*-t_{rac}-*lacZYA* cassette as a single-copy lysogen at the λ attachment site. It was made *rpoC*^{ts} by P1 transduction (*rpoC*, β' gene), resulting in strain RS1606. The P_{RM}-*racR*-t_{rac}-*lacZYA* cassette was inserted at the λ attachment site of RS1714 that produces ρ^{Y80C} by λRS45 phage-mediated transduction, resulting in RS1729. This strain was subsequently made *rpoC*^{ts} by P1 transduction to construct RS1758.

Plasmid pBAD18M containing *rpoC*^{WT} was transformed into the XL1-red mutator strain (*67*). A mutagenized plasmid library was isolated and electroporated into RS1758. After plating on LB agar, transformants were transferred to MacConkey-lactose plates and grown at 37 °C. Synthetically defective *rpoC* mutants were identified as red colonies (*lac*+ phenotype). ~100,000 colonies were screened. Plasmids were isolated and sequenced to identify mutations in *rpoC*. This screening yielded one positive mutant, *rpoC-G82D.* Additonal *rpoC* mutants were constructed by site-directed mutagenesis of pBAD18M-$rpoC^{WT}$.

To assess synthetic growth defects, strains RS1606 (ρ^{WT}) and RS1758 (ρ^{Y80C}) were transformed with the pBAD18M plasmids expressing WT or mutant *rpoC*. Transformants were streaked at 30, 37, and 42 °C. The chromosomal $rpoC^{ts}$ allele is inactive at 37 °C and above. *rpoC* mutant strains exhibiting clear growth defects with ρ^{Y80C} were spotted in serial dilutions on LB agar plates and incubated at 37 °C to further quantify the synthetic growth defects. To estimate termination defects of ρ^{WT} and ρ^{Y80C} in the presence of β' variants, we quantified β-gal produced from the P_{RM}-t_{rac}-*lacZYA* terminator fusion cassette using strains RS1606 (ρ^{WT}) and RS1758 (ρ^{Y80C}) at 37 °C (*68*).

Quantification and statistical analysis

For quantification of experimental results based on gel analyses, at least three independent experiments were conducted using the same biochemical samples. Gels were scanned using a Typhoon FLA 9000 PhosphorImaging system (GE Healthcare Life Sciences). RNA products were quantified with ImageQuant. Means, SD, and t-test values were calculated using Excel (Microsoft). Error analyses for the β-galactosidase and growth assays were also performed using Excel.

Supplementary Figures

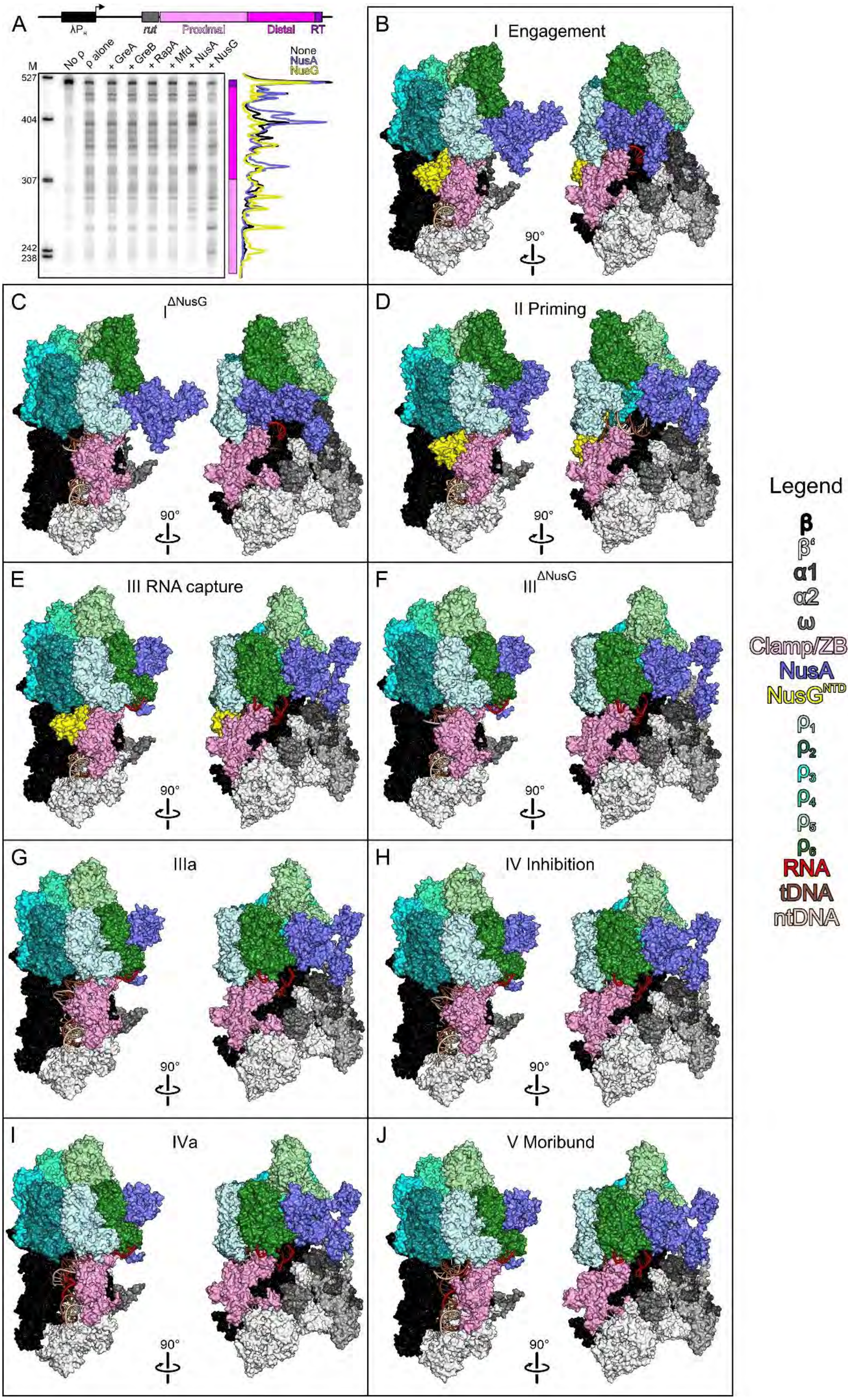

Fig. S1. ρ terminates NusA/NusG-modified ECs. (**A**) Schematic of the λ tR1 DNA template and effects of ρ on single-round *in vitro* transcription by *E. coli* RNAP alone or in the presence of the indicated general transcription factors. In this and the following figures: RT, readthrough; M, pBR322 *Msp*I marker (nts); proximal termination zone, pink; distal termination zone, magenta; RT, purple. Right, gel traces for ρ acting on RNAP alone (black), with NusA (slate blue), or with NusG (yellow); traces with other factors were superimposable with that of RNAP alone. (**B-J**) Orthogonal surface views (nucleic acids as cartoon) of the indicated complexes. Key elements are labeled. Complexes were superimposed based on the β subunits. dDNA, downstream DNA; prox./dist. uDNA, proximal/distal upstream DNA. Color-coding in this and the following figures: RNAP subunits, different shades of gray; β’ clamp, pink; ρ subunits, different shades of green/cyan; NusA, slate blue; NusG, yellow; template DNA, brown; non-template DNA, beige; RNA, red.

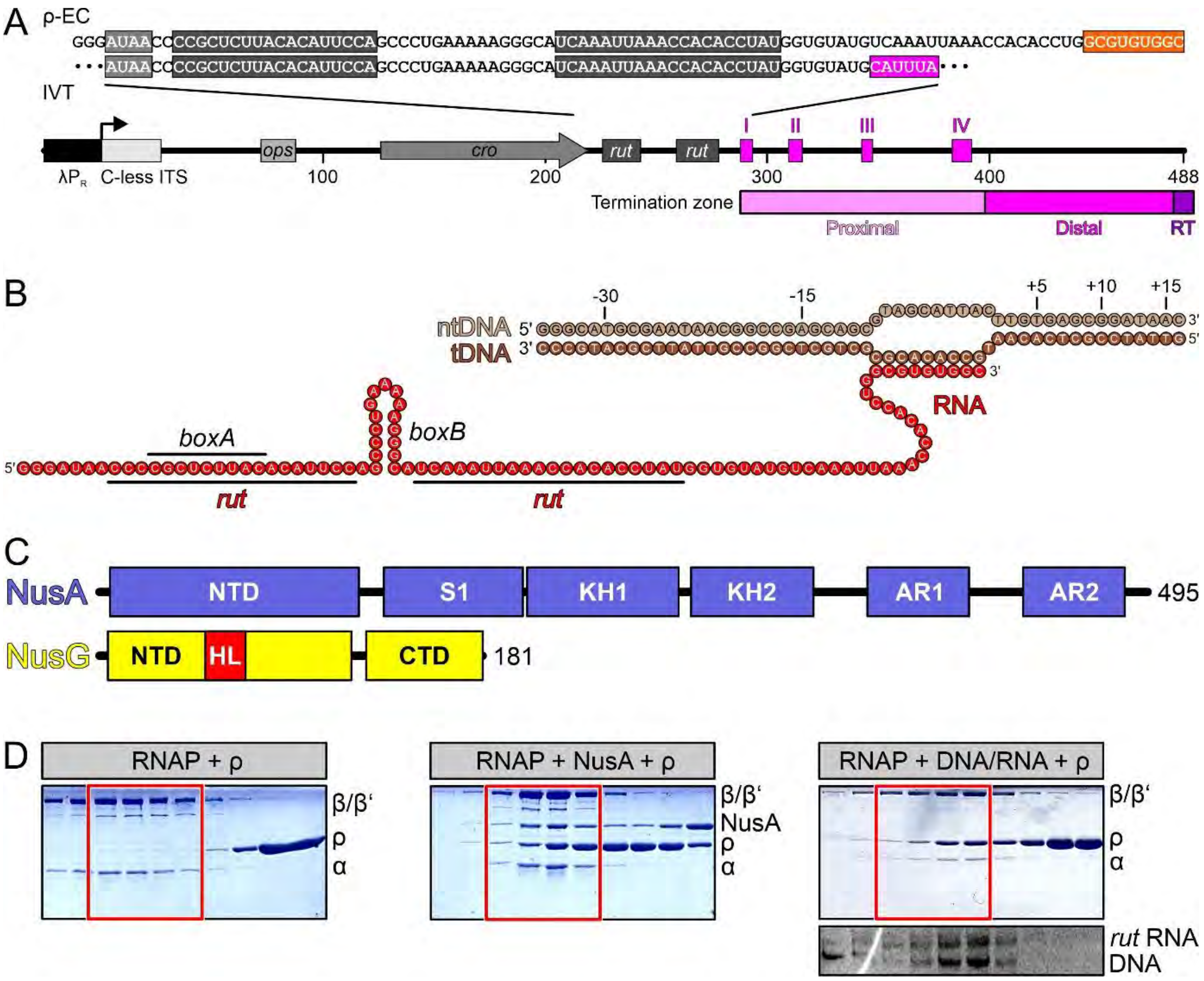

Fig. S2. Nucleic acids, proteins, ρ recruitment and EC inhibition. (**A**) Schematic of the λ tR1 DNA template used for *in vitro* transcription (IVT) assays in this and previous studies (*13, 69*). RNAP that initiates at the λ P$_R$ promoter is stalled at the end of an initial transcribed sequence (ITS) in the absence of CTP, allowing synchronization of ECs for single-round assays. Positions of the *rut* sites, the proximal and distal termination windows, and the RT RNA are indicated; major release sites I/II/III/IV (*69*) are shown. Sequences of *rut* RNA regions transcribed from this template (IVT) and used to assemble ρ-ECs for cryoEM analysis (ρ-EC) are shown at the top; the 3'-segment of RNA that anneals to the tDNA is boxed in orange. (**B**) Nucleic acid scaffold used for the assembly of ρ-ECs. The *boxA*/*boxB* RNA elements employed in the assembly of the phage λ anti-termination complex (*24*) are also shown. (**C**) Domain organization of NusA and NusG. HL, NusG HL; numbers, C-terminal residues. (**D**) SDS-PAGE (proteins) and urea-PAGE (nucleic acids) gels monitoring ρ binding to RNAP (left), RNAP/NusA (middle) and unmodified EC (right). Red boxes indicate identical fractions of the runs, in which RNAP peaks.

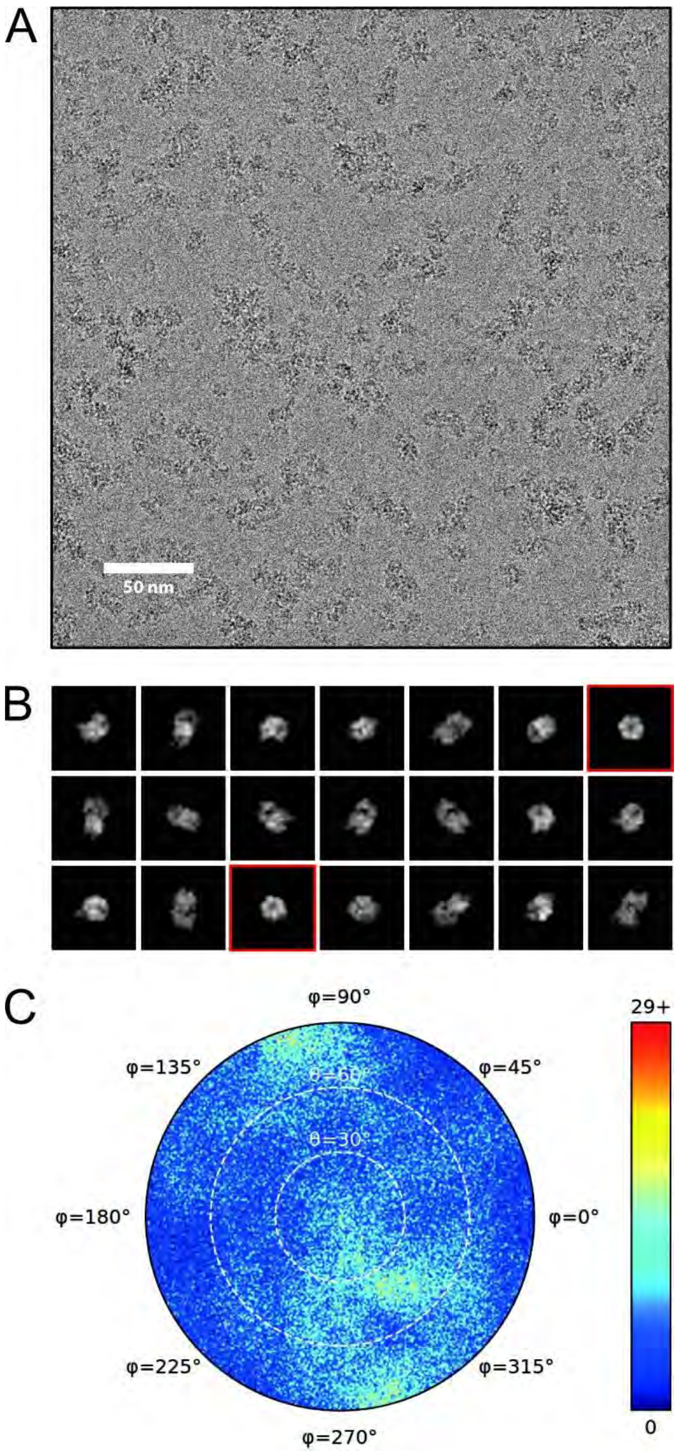

Fig. S3. CryoEM imaging of ρ-ECs. (**A**) Representative cryoEM micrograph of ρ-ECs. Scale bar, 50 nm. Well-separated particles are predominant. Particles with different views can be seen, suggesting random orientation. (**B**) Top 2D class averages of the ρ-ECs. Views from all sides of the complex can be found. In the top views, the ρ hexamer can be discerned (red boxes). (**C**) Angular distribution plot of the homogeneously refined ρ-EC used for subsequent classification with cisTEM, revealing an even distribution of viewing directions with only limited preference.

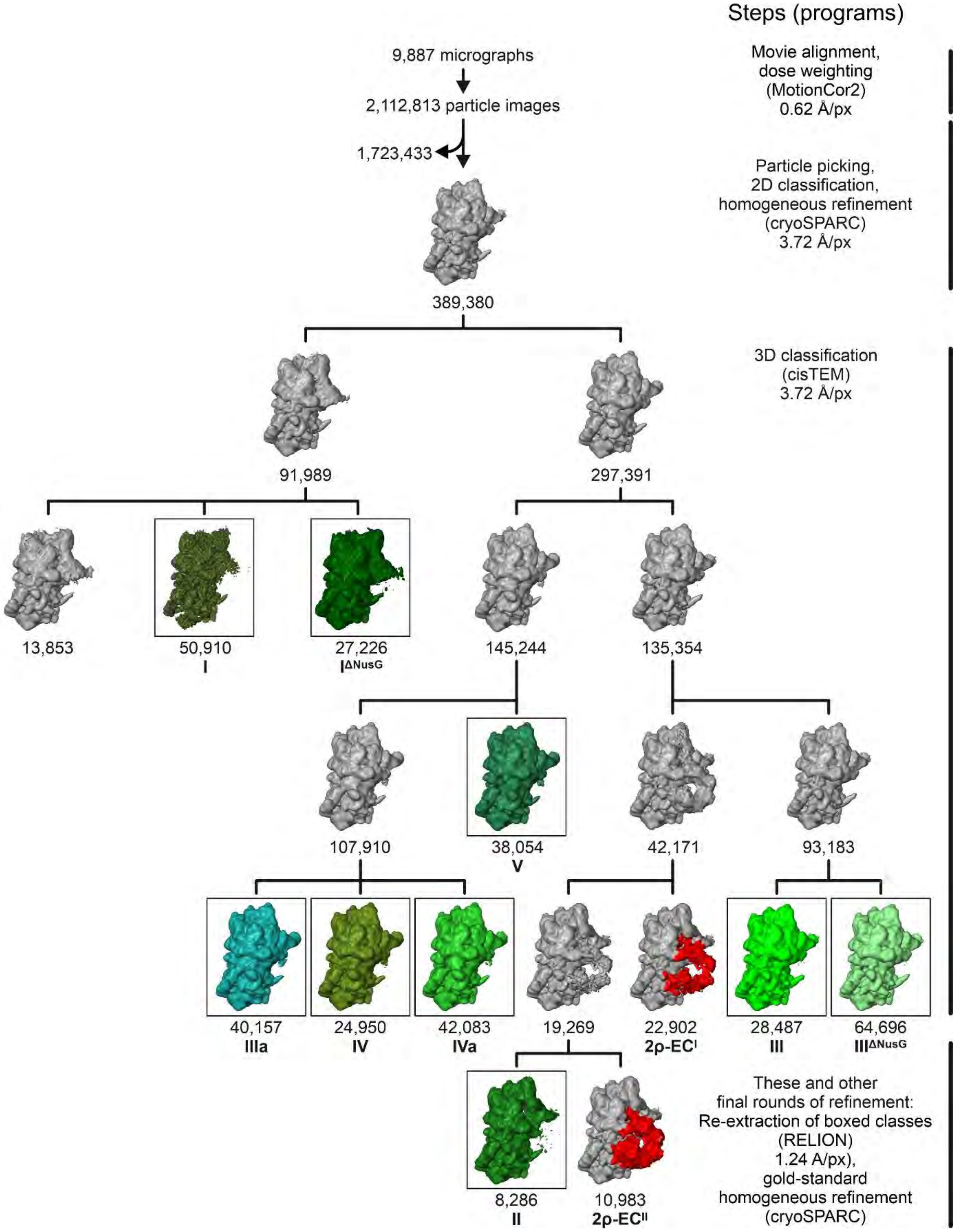

Fig. S4. Hierarchical clustering analysis. A total of 9887 micrographs was used to iteratively select 389,380 particle images representing ρ-ECs. In subsequent 3D classification cycles without refinement, separation was first based on global differences, such as the rotational state of the ρ hexamer, followed by focused classification on local differences, using spherical masks enclosing the region of interest. Boxed structures in shades of green represent the nine final classes used for further structural analyses in this study (names indicated). Two additional classes, 2ρ-EC^{I} and 2ρ-EC^{II}, have weak cryoEM density for a second ρ hexamer (colored red) bound to NusA and the RNAP β’ jaw in addition to ρ observed at the main position. Although higher-order ρ oligomers had been reported *in vitro* (*70*), determining whether two ρ hexamers can act on the same EC *in vivo* is beyond the present scope of our manuscript. For better visualization, all maps were filtered to 8 Å resolution.

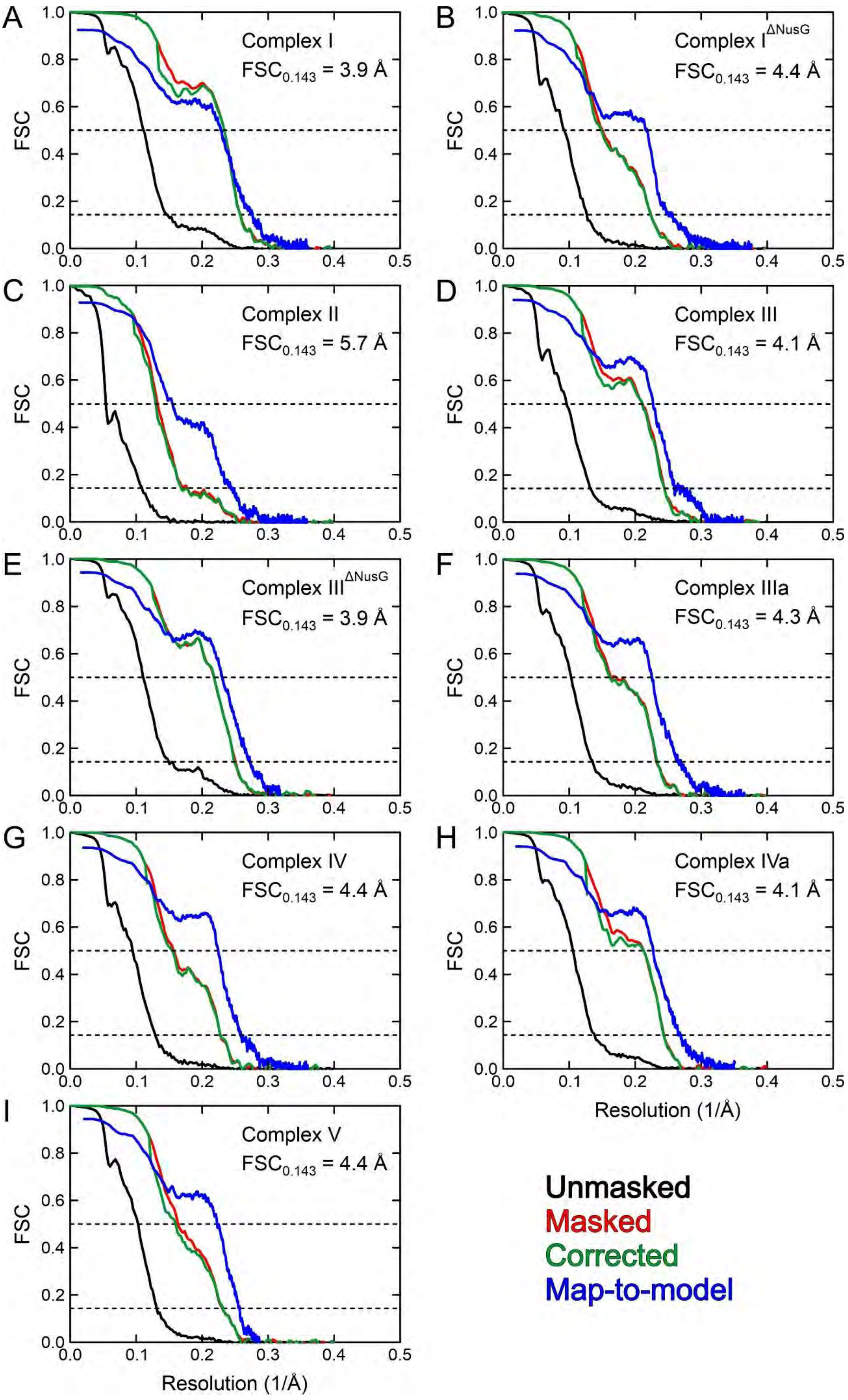
A
Complex I
$FSC_{0.143}$ = 3.9 Å
B
Complex $I^{\Delta NusG}$
$FSC_{0.143}$ = 4.4 Å
C
Complex II
$FSC_{0.143}$ = 5.7 Å
D
Complex III
$FSC_{0.143}$ = 4.1 Å
E
Complex $III^{\Delta NusG}$
$FSC_{0.143}$ = 3.9 Å
F
Complex IIIa
$FSC_{0.143}$ = 4.3 Å
G
Complex IV
$FSC_{0.143}$ = 4.4 Å
H
Complex IVa
$FSC_{0.143}$ = 4.1 Å
I
Complex V
$FSC_{0.143}$ = 4.4 Å
FSC
1.0
0.8
0.6
0.4
0.2
0.0
0.0
0.1
0.2
0.3
0.4
0.5
Resolution (1/Å)
Unmasked
Masked
Corrected
Map-to-model

Fig. S5. Resolution limits. (**A-I**) Global resolution estimates represent gold-standard Fourier-shell correlation (FSC) after refinement with cryoSPARC2 (*61*) of the nine refined complexes (names indicated). Global resolutions vary between 3.9 Å for complexes I and III$^{\Delta\text{NusG}}$ and 5.7 Å for complex II. Black curves were calculated without masking. Red curves were calculated after application of a soft solvent mask dilated by 6 Å. Green curves were calculated with phase randomization to correct for mask-induced correlations. Blue curves represent cross-resolutions between the refined model and the experimental electron density as determined with PHENIX.

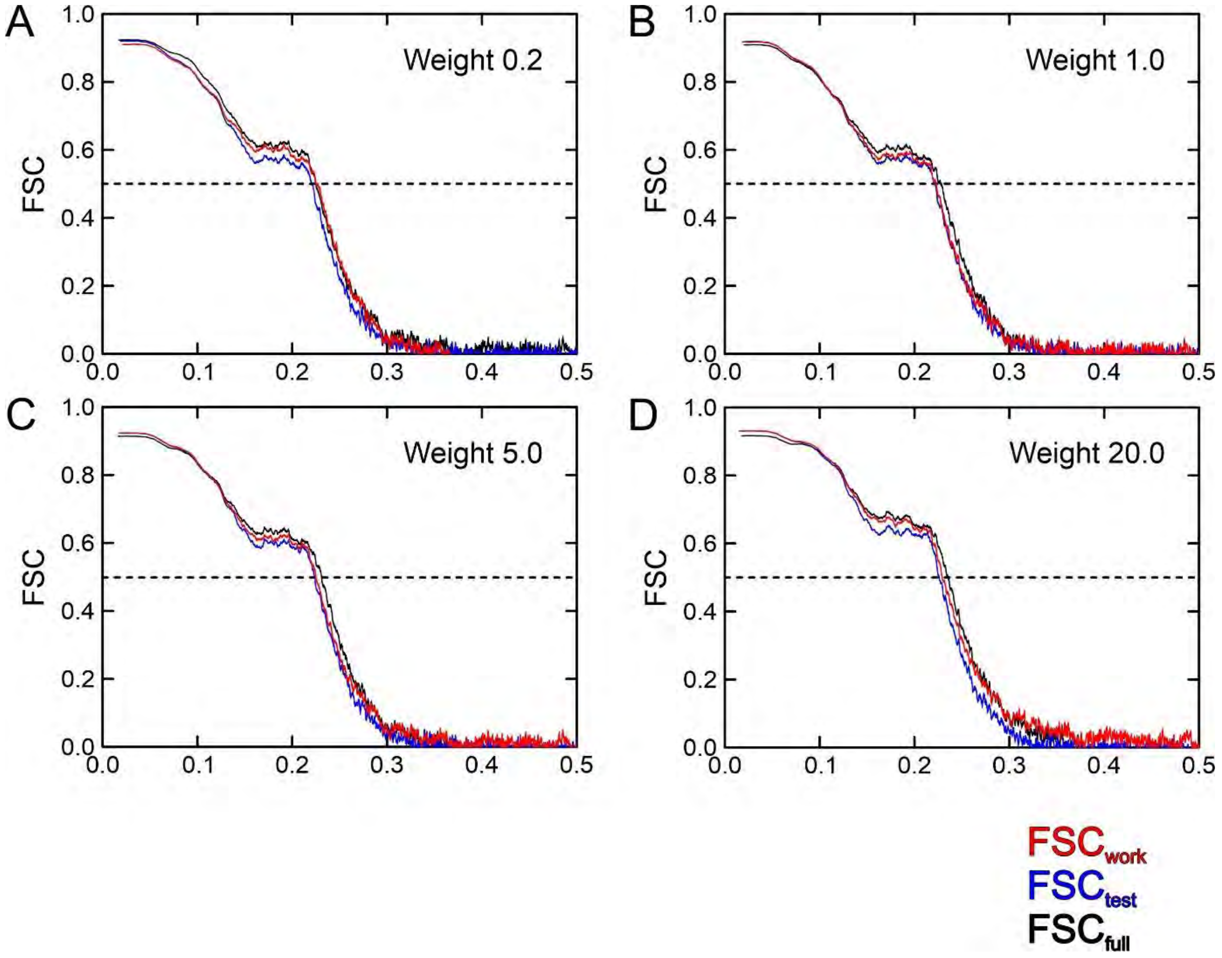

Fig. S6. Monitoring of overfitting during real-space refinement. (**A-D**) Example (complex I) for the optimization of weighting between geometry restraints and electron density map during real space refinement in PHENIX. Cross-resolution between the half-map used for refinement and refined model (FSC_{work}, red line) is compared with the cross-resolution between refined model and the unused half-map (FSC_{test}, blue line). Final refinement was carried out against the full map utilizing all particle images (FSC_{full}, black line). The tested weighting factors were 0.2 (**A**), 1 (**B**), 5 (**C**) and 20 (**D**). Deviations between FSC_{work} and FSC_{test} indicate overfitting of the model, showing minimal overfitting for a weight of 1.

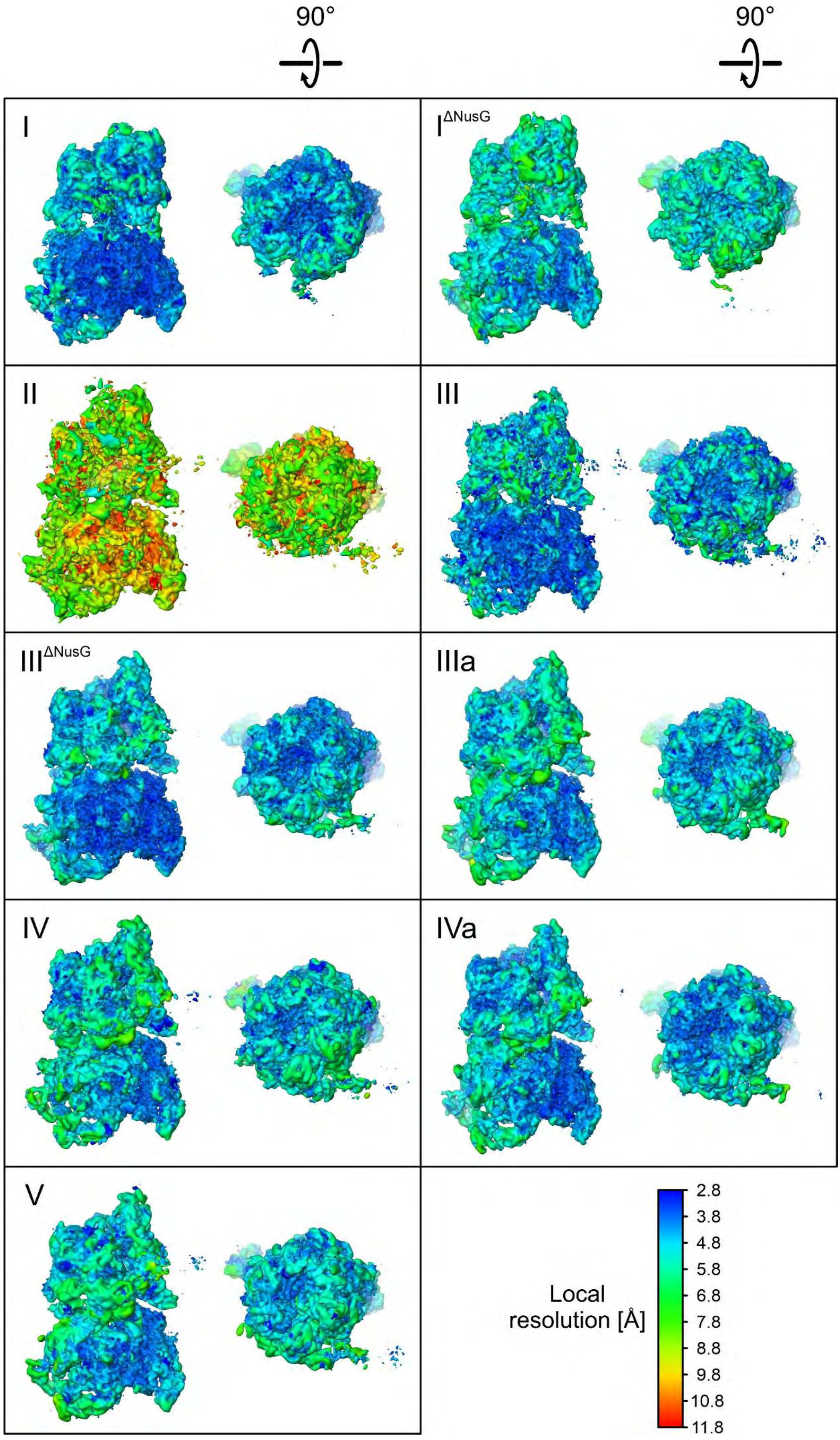
90°
90°
I
IΔNusG
II
III
IIIΔNusG
IIIa
IV
IVa
V
Local resolution [Å]
2.8
3.8
4.8
5.8
6.8
7.8
8.8
9.8
10.8
11.8

Fig. S7. Local resolutions. CryoEM maps of the nine refined complexes (names indicated) colored by local resolutions (see legend) as estimated by cryoSPARC2. Local resolutions show variations across the reconstructions for all complexes, ranging from below 3 Å in some RNAP cores to 8-12 Å in some peripheral regions. For display, maps were filtered according to local resolution estimates.

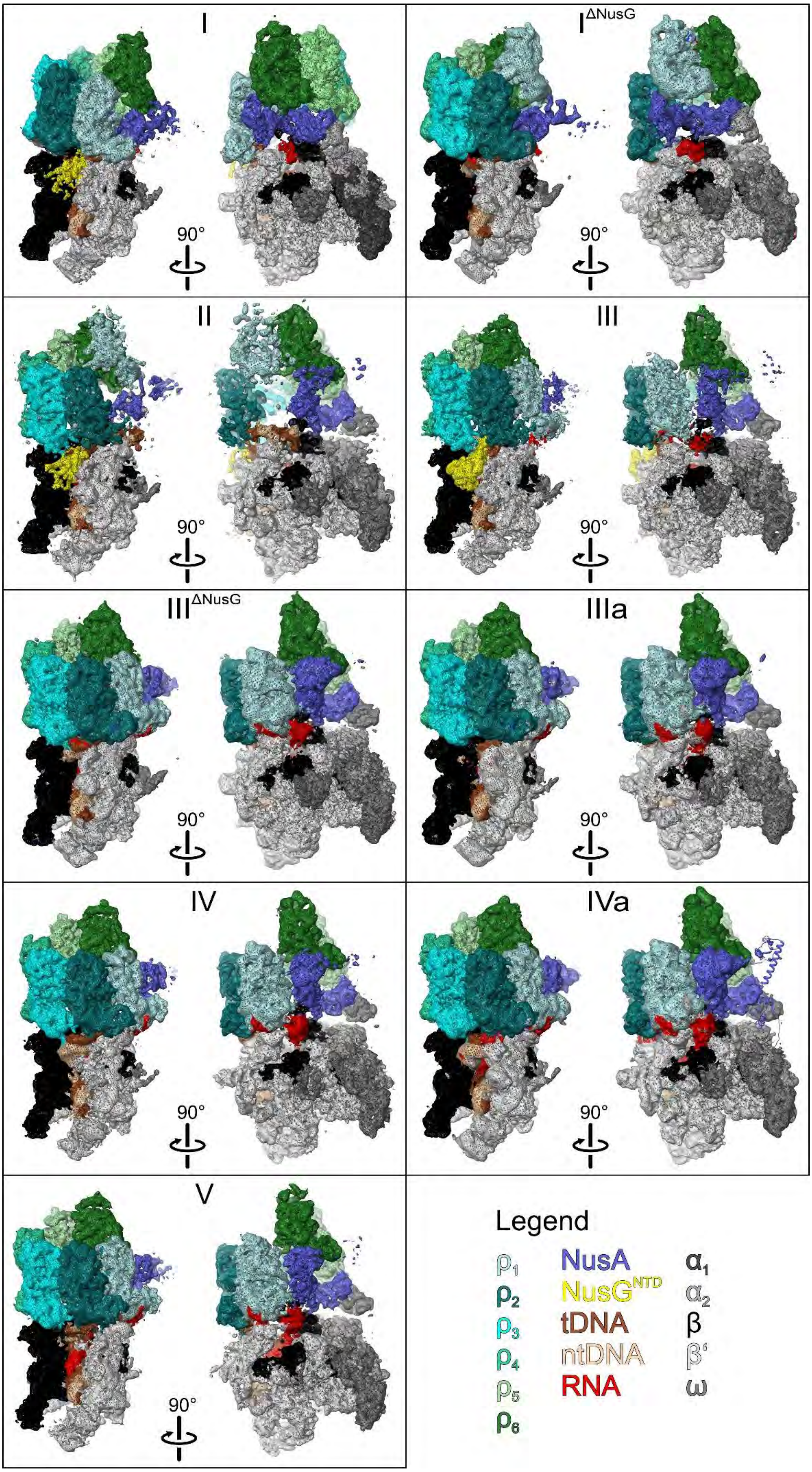
I
90°
$I^{\Delta NusG}$
90°
II
90°
III
90°
$III^{\Delta NusG}$
90°
IIIa
90°
IV
90°
IVa
90°
V
90°
Legend
ρ_1
ρ_2
ρ_3
ρ_4
ρ_5
ρ_6
NusA
$NusG^{NTD}$
tDNA
ntDNA
RNA
α_1
α_2
β
β'
ω

Fig. S8. Global cryoEM densities. Orthogonal views of cryoEM densities filtered to local resolutions for the nine refined complexes (names indicated). Same views as in Fig. S1B-J. None of the maps revealed density for NusG^{CTD}, and similar structures were obtained from complexes assembled with NusG lacking the CTD. The C-terminal NusA AR1 and AR2 domains were poorly resolved in reconstructions and were tentatively placed into regions of "fuzzy" density, based on their known positions in ECs (*22-24*). We could clearly assign RNA in the hybrid and close to the RNA exit tunnel next to the β'^{ZBD}.

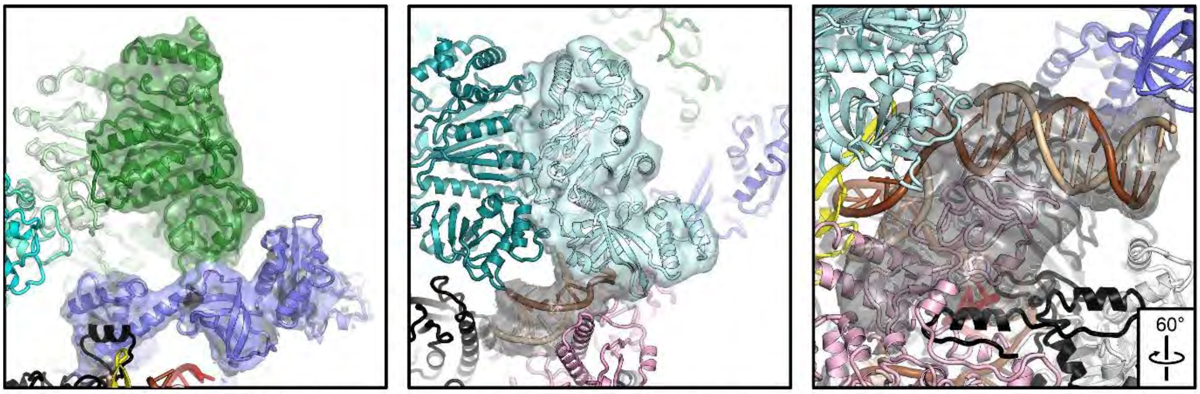

I: ρ_6 and NusA$^{\text{NTD-S1-KH}}$ **I$^{\Delta\text{NusG}}$**: ρ_1 and uDNA **II**: ZBD and dist. uDNA

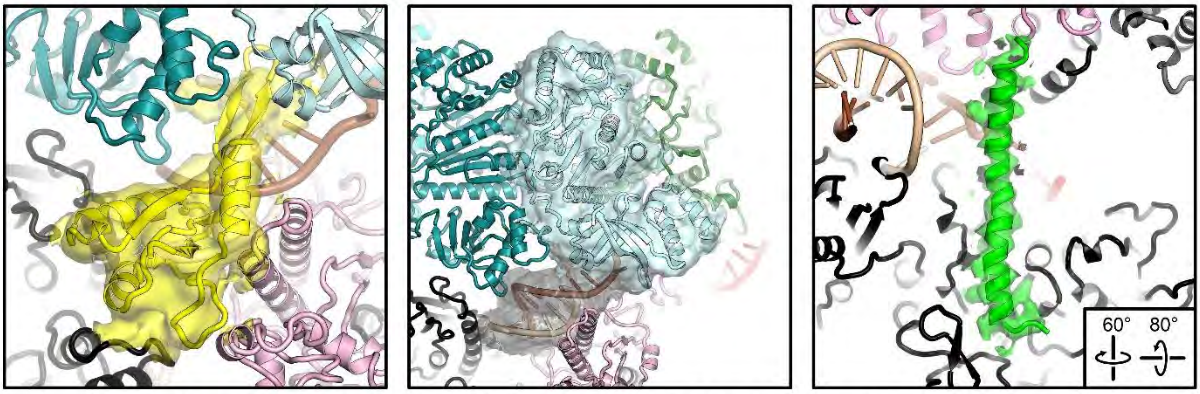

III: NusG **III$^{\Delta\text{NusG}}$**: ρ_1 and uDNA **IIIa**: Bridge helix

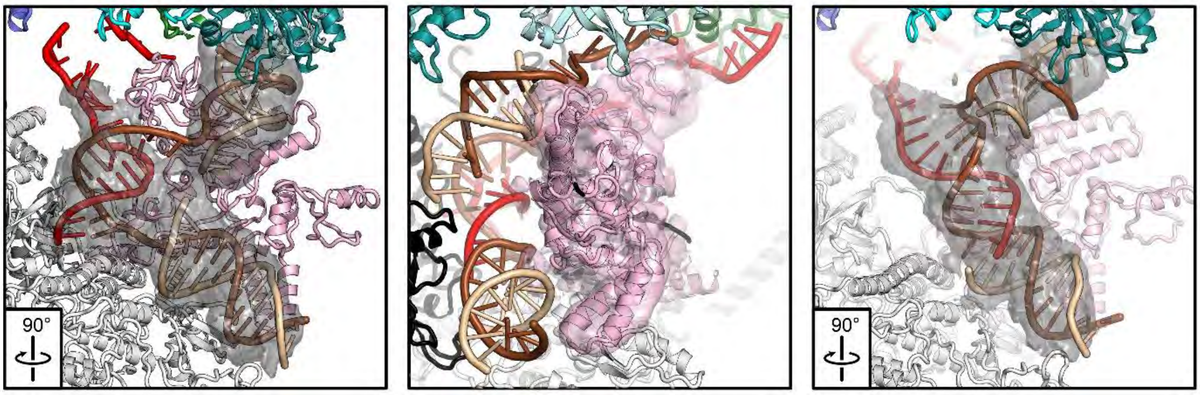

IV: dDNA, hybrid, uDNA **IVa**: Clamp **V**: dDNA, hybrid, uDNA

Fig. S9. Local cryoEM densities. Selected regions of the cryoEM densities of the nine refined complexes filtered to the local resolution. Complexes and regions shown are identified below the panels.

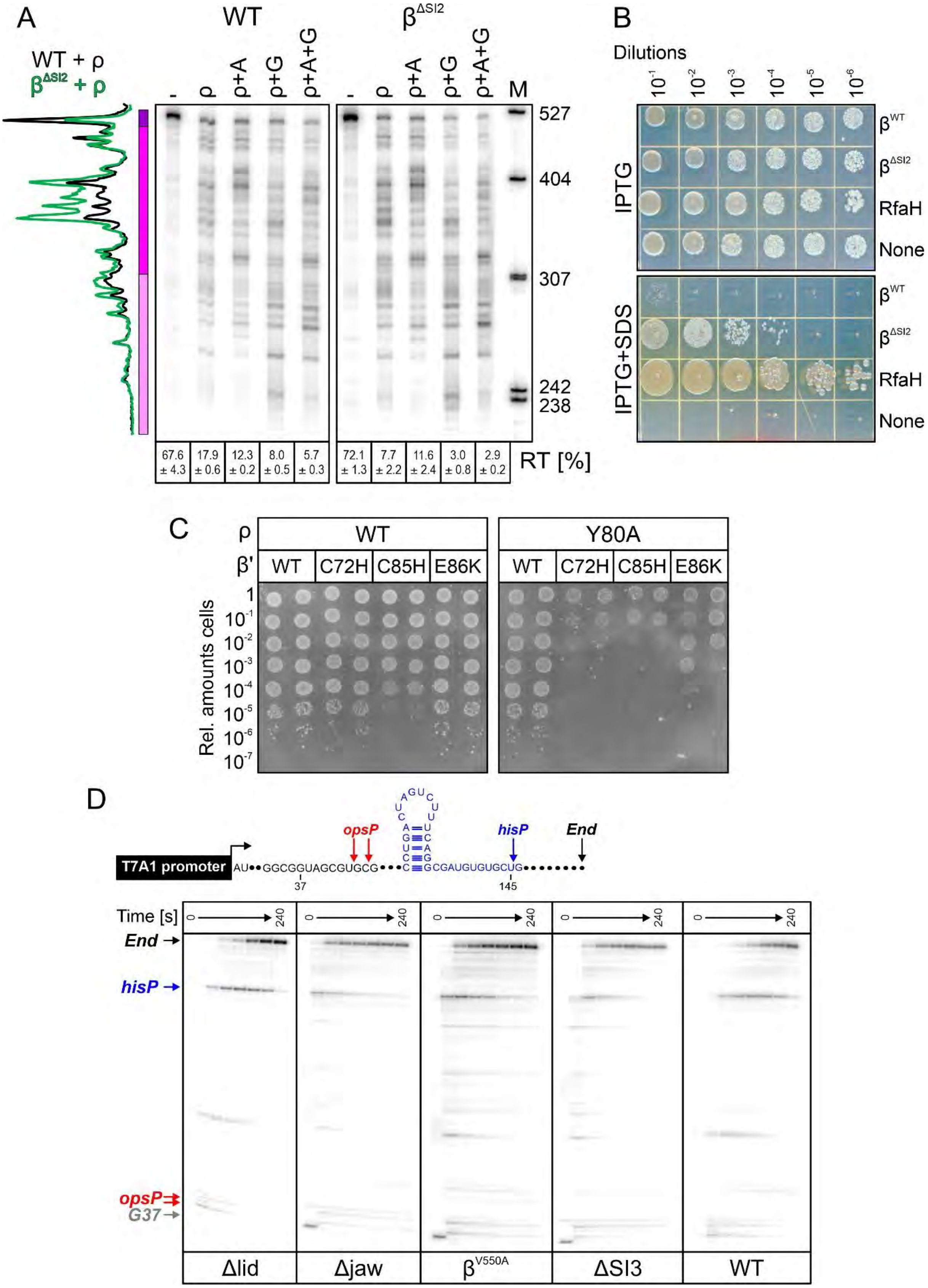
A
WT + ρ
β^ΔSI2 + ρ
WT
β^ΔSI2
-
ρ
ρ+A
ρ+G
ρ+A+G
M
527
404
307
242
238
67.6 ± 4.3
17.9 ± 0.6
12.3 ± 0.2
8.0 ± 0.5
5.7 ± 0.3
72.1 ± 1.3
7.7 ± 2.2
11.6 ± 2.4
3.0 ± 0.8
2.9 ± 0.2
RT [%]
B
Dilutions
10^-1
10^-2
10^-3
10^-4
10^-5
10^-6
IPTG
IPTG+SDS
β^WT
β^ΔSI2
RfaH
None
C
ρ
β'
WT
Y80A
WT
C72H
C85H
E86K
Rel. amounts cells
1
10^-1
10^-2
10^-3
10^-4
10^-5
10^-6
10^-7
D
T7A1 promoter
AU••GGCGGUAGCGUGCG•••C≡GCGAUGUGUGCUG••••••••
37
145
opsP
hisP
End
Time [s]
0
240
End
hisP
opsP
G37
Δlid
Δjaw
β^V550A
ΔSI3
WT

Fig. S10. Effects of RNAP variants on pausing and termination *in vitro* and growth *in vivo*. (**A,B**) Effects of β SI2 deletion on ρ termination *in vitro* (**A**) and *in vivo* (**B**). *In vivo* termination was assayed in MG1655 Δ*rfaH* strain in which resistance to SDS depends on reduced ρ termination in the *waa* operon (*71*). Serial dilution of cells carrying plasmids with indicated proteins expressed from an IPTG-inducible P_{trc} promoter (or an empty vector) were spotted on LB agar plates supplemented with carbenicillin and IPTG (with or without 0.5 % SDS) and incubated at 37 °C. (**C**) Synthetic growth defects observed for three representative β' variants (C72H, C85H, E86K) quantified using a spotting assay. Equal volumes of several dilutions (left) of saturated cultures were spotted on LB agar plates and incubated at 37 °C. (**D**) Effects of deleting the β' lid (Δlid), jaw (Δjaw), or SI3 (ΔSI3), or of β^{V550A} on RNAP pausing during single-round transcription of an *ops*/*his* pause-containing template (scheme on top) *in vitro*. Consistent with earlier studies (*41, 42, 72, 73*), the deletion of the β' lid did not alter elongation properties of RNAP, whereas the deletions of the β' jaw and SI3, as well as β^{V550A} substitution led to defects in pausing.

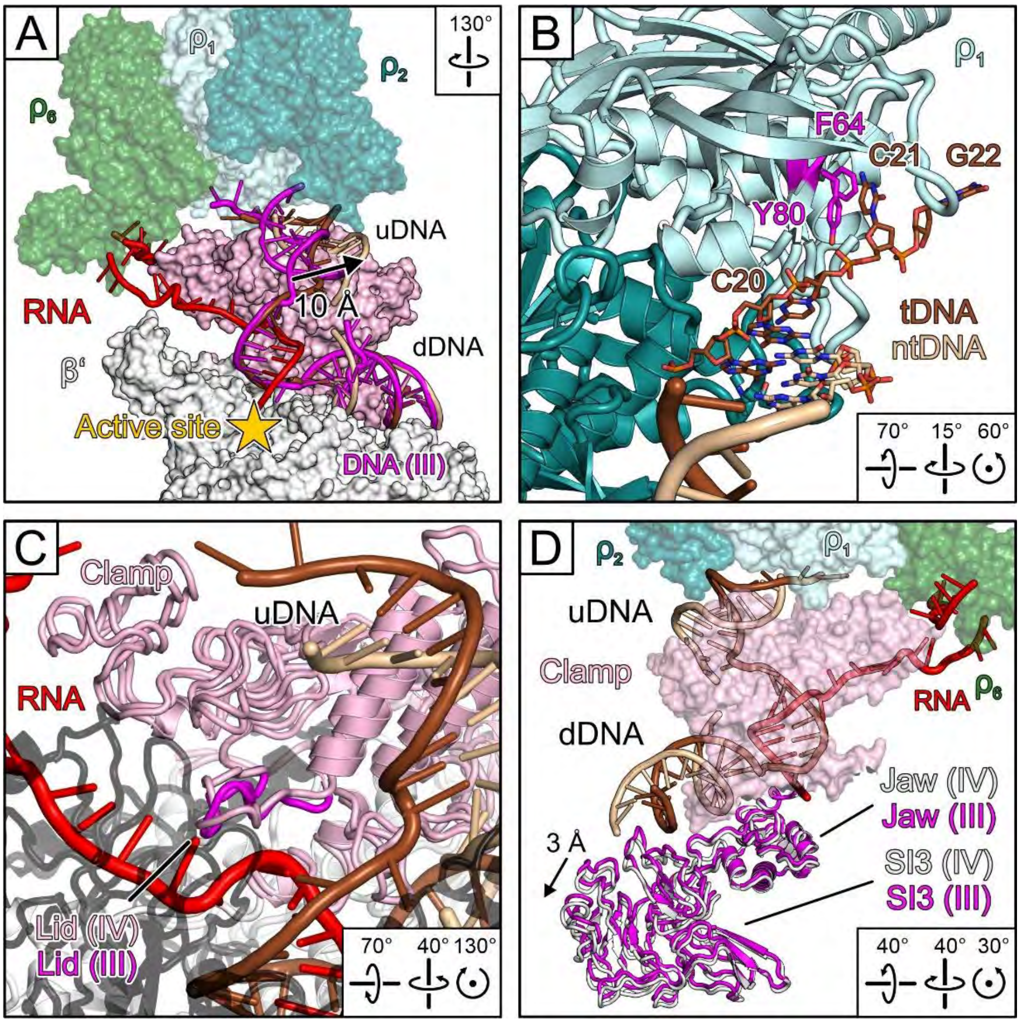

Fig. S11. Inhibition and moribund complex. (**A, C, D**) Comparison of selected elements of the inhibited complex (regular colors) with selected elements of the RNA capture complex (magenta), illustrating movement (arrows) of the proximal uDNA that is in conflict with NusG^{NTD} binding (**A**), rearrangement of the lid (**C**), and movement of β' jaw and SI3 (**D**). (**B**) Partial retraction of the DNA template strand from the ρ_1 PBS. tDNA and selected ρ_1 PBS residues as sticks colored by atom type. Carbon tDNA, brown.

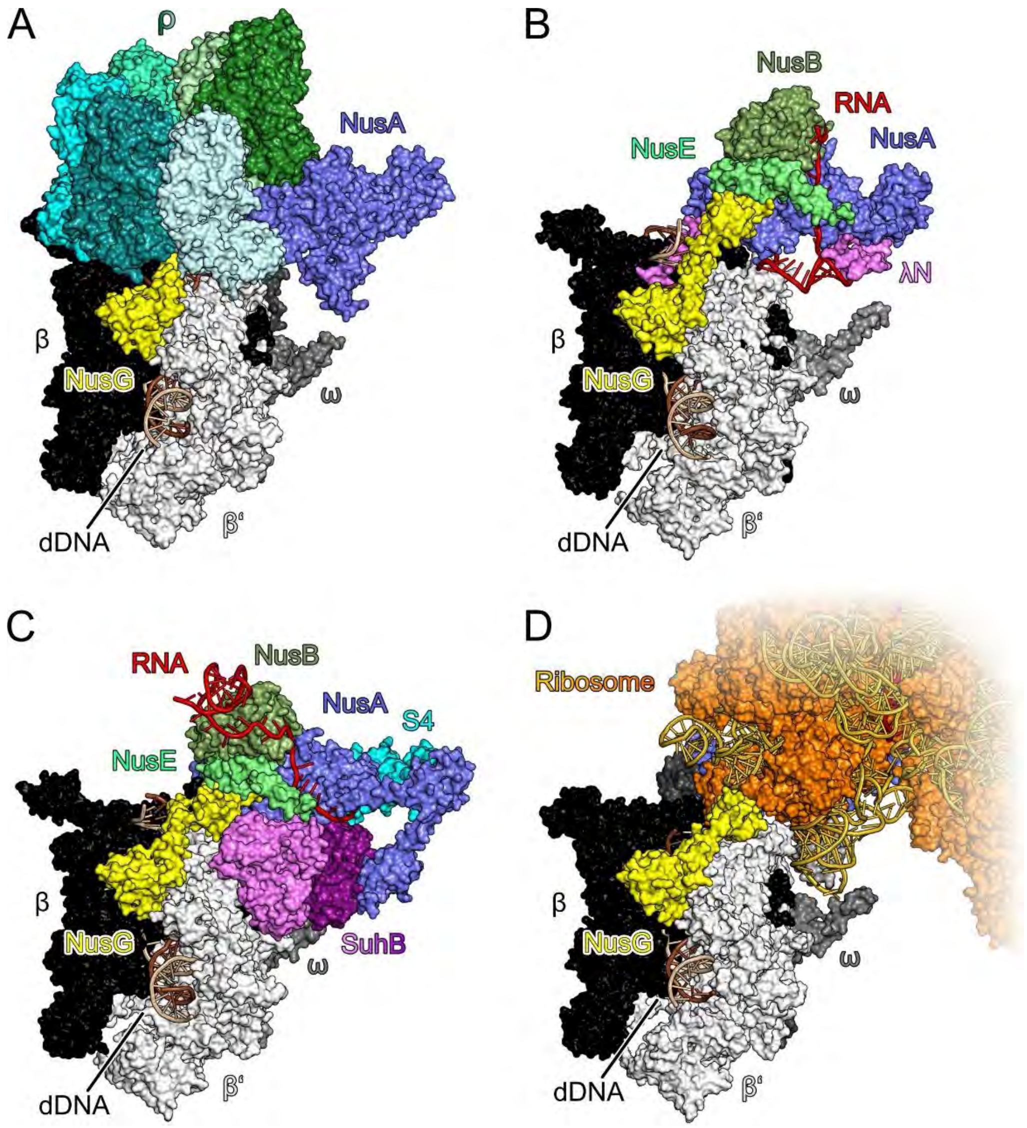

Fig. S12. Comparison to anti-termination complexes and expressomes. (**A-D**) Side-by-side comparison of the structures of the engagement complex (**A**), a λN-based anti-termination complex (λN-TAC; PDB ID 6GOV) (*24*) (**B**), a ribosomal RNA EC (*rrn*EC; PDB ID 6TQN) (*23*). (**C**), and an expressome (PDB ID 6X7K) (*37*). (**D**). Structures were superimposed based on the β subunits. RNAP-associated RNA-factor complexes in the λN-TAC and *rrn*EC, or the ribosome in expressomes (*37, 38, 74*) physically block EC engagement by ρ as revealed in the structures described here. ρ competition by a closely trailing ribosome provides an explanation for the long-known polarity effect (*75*), *i.e.* stalling of translation on an upstream gene in an operon leading to downregulation of transcription in downstream genes.

Supplementary Tables

Table S1.

Cryo-EM data collection and refinement.

Data Collection	
Pixel size (Å/px)	1.24
Defocus range (µm)	0.5-2.5
Voltage (kV)	300
Electron dose (e$^-$/A^2)	50
Number of frames	50
Micrographs	9887

Refinement									
Class	**I**	**II**	**III**	**IV**	**V**	**$\text{I}^{\Delta\text{NusG}}$**	**$\text{III}^{\Delta\text{NusG}}$**	**IIIa**	**IVa**
Particle images	50,910	8,286	28,487	24,950	38,054	27,226	64,696	40,157	42,083
Global resol. [Å][1]	3.9	5.7	4.1	4.4	4.4	4.4	3.9	4.3	4.1
Local resol. [Å][1]	2.4-7.8	2.3-10.5	2.7-8.4	2.6-9.6	2.7-9.6	2.6-10.5	2.7-10.3	2.7-10.5	2.7-10.5
CC mask	0.73	0.79	0.79	0.77	0.76	0.72	0.79	0.76	0.77
CC volume	0.68	0.79	0.78	0.76	0.75	0.72	0.79	0.76	0.76
Model composition									
Non-H atoms	52,293	52,592	52,418	51,610	51,405	51,365	51,565	51,610	51.553
Protein residues	6,443	6,442	6,442	6,330	6,315	6,331	6,330	6,330	6,315
DNA residues	59	84	60	61	57	58	59	61	60
RNA residues	17	9	28	28	28	17	28	28	32
Zn^{2+} / Mg^{2+} ions	2 / 7	2 / 6	2 / 6	2 / 6	2 / 6	2 / 7	2 / 6	2 / 6	2 / 6
ADP-BeF$_3$	6	5	5	5	5	6	5	5	5
RMSD[2]									
Bond lengths [Å]	0.003	0.002	0.002	0.002	0.003	0.003	0.002	0.002	0.002
Bond angles [°]	0.598	0.605	0.581	0.568	0.625	0.593	0.546	0.530	0.536
Ramachandran plot									
Favored [%]	94.9	96.1	95.7	95.3	94.8	95.2	95.4	95.8	95.3
Allowed [%]	5.1	3.9	4.3	4.7	5.2	4.8	4.6	4.2	4.6
Outliers [%]	0.0	0.0	0.0	0.0	0.0	0.0	0.0	0.0	0.0
Model quality[3]									
Clash score	15.3	16.8	4.1	12.5	15.9	13.8	12.8	13.1	13.2
Rotamer outl. [%]	5.2	4.8	6.1	4.7	5.7	4.1	3.8	3.5	3.1
Overall score	2.6	2.5	2.5	2.4	2.6	2.5	2.4	2.3	2.3
EMDB ID	11087	11088	11089	11090	11091	11722	11723	11724	11725
PDB ID	6Z9P	6Z9Q	6Z9R	6Z9S	6Z9T	7ADB	7ADC	7ADD	7ADE

[1] FSC$_{0.143}$ criterion.
[2] RMSD – root-mean-square deviation from ideal geometry.
[3] Assessed using MolProbity (*76*).

Table S2.

Regions of RNAP and factors discussed in the text.

RNAP	
β	
Element	Residue range
β1-lobe (protrusion)	31-139/456-512
β2-lobe: βi4 (lobe:SI1)	151-444
β SI1	226-350
β gate loop	359-388
β protrusion	450-507
β connector	814-839/1048-1065
β flap	830-1058
β flap tip	887-915
β flap tip arms	890-899/910-914
β SI2	938-1040
C-terminal β clamp	1233-1342
β clamp	1241-1341
β'	
Element	Residue range
β' ZBD	35-107
β' zipper	36-61
β' clamp	16-342/1318-1344
N-terminal β' clamp	132-190
β' lid	250-264
β' clamp helices	265-307
β' rudder	308-327
β' switch 2	330-349
β' dock	369-420
β' shelf	787-931
β' SI3	943-1130
β' jaw	1135-1317
β'C	1318-1375
α	
Element	Residue range
NTD	6-232
NTD-CTD linker	233-251
CTD	252-321
ω	
Element	Residue range
Globular domain	1-60
C-terminal helix	61-91
Factors	
NusA	
Element	Residue range
NTD	1-121
NTD-S1 linker helix*	104-132
S1	133-200
KH1	201-277
KH2	278-339
KH2-AR1 linker helix	340-363*
AR1	354-416
AR1-AR2 linker helix	400-428
AR2	429-495
NusG	

Element	Residue range
NTD	4-119
HL	46-65
NTD-CTD linker	120-125
CTD	126-181
ρ	
Element	Residue range
NTD	1-128
NTD-CTD linker	129-140
CTD	141-419

* The N-terminal part of the NTD-S1 linker helix is also part of the NTD; the C-terminal part of the KH2-AR1 linker helix is also part of AR1.

Table S3.

Growth defects of β'^{ZBD} variants in the presence of ρ^{Y80C}.

ρ	**WT**			**Y80C**		
T [°C]	**30**	**37**	**42**	**30**	**37**	**42**
WT	++++	++++	++++	++++	++++	+/-
C70A	++++	++	+	++++	+	-
C70H	++++	++	+	++++	+	-
C72A	++++	++	+	++++	-	-
C72H	++++	++++	+/-	++++	-	-
Y75N	++++	++++	++++	++++	++++	+/-
G82D	++++	++++	++++	++++	++++	+/-
C85A	++++	++	+	++++	+	-
C85H	++++	++++	+	++++	+	-
E86K	++++	++++	+++	++++	+	-
C88A	++++	++	+	+++	-	-
C88H	++++	++	++	+++	++	-
C2A[1]	++++	++	++	+++	++	-
C3A[2]	++++	++	++	+++	-	-
C4A[3]	++++	++	++	+++	-	-

[1] C2A: C70A-C72A

[2] C3A: C70A-C72A-85A

[3] C4A: C70A-C72A-C85A-C88A.

Table S4.

Plasmids used for protein production.

Plasmid	Relevant Features	Reference
pVS10	*E. coli* wild-type RNAP expression construct	(*55*)
pET24b-NusG	*E. coli* NusG$^{\mathrm{FL}}$ expression construct	(*13*)
pGEX-6p1-NusG	*E. coli* NusG$^{\mathrm{FL}}$ expression construct	(*57*)
pET24b-NusG NTD	*E. coli* NusG$^{\mathrm{NTD}}$ expression construct	(*13*)
pMT037	*E. coli* NusG$^{\Delta\mathrm{HL}}$ expression construct	This study
pET24b-Rho	*E. coli* Rho expression construct	(*13*)
pETM11-Rho	*E. coli* Rho expression construct	(*24*)
pTKK19_NusA	*E. coli* NusA expression construct	(*77*)
pETM11-NusA	*E. coli* NusA$^{\mathrm{FL}}$ expression construct	(*57*)
pIA578	*E. coli* GreA expression construct	(*78*)
pIA579	*E. coli* GreB expression construct	(*78*)
pAD6	*E. coli* Mfd expression construct	(*79*)
pGB003	*E. coli* RapA expression construct	This study
pIA1159	*E. coli* RNAP Δα CTD expression construct	This study
pIA314	*E. coli* RNAP Δβ SI2 expression construct	(*80*)
pAM022	*E. coli* RNAP β V550A expression construct	(*41*)
pVS14	*E. coli* RNAP Δβ’ SI3 expression construct	(*42*)
pIA299	*E. coli* RNAP Δω expression construct	(*80*)
pIA1024	*E. coli* RNAP Δβ’ jaw expression construct	(*81*)
pHM001	*E. coli* RNAP Δβ lid expression construct	(*82*)
pIA267	λ tR1 template for *in vitro* termination assays	(*69*)

Table S5.

E. coli strains and plasmids used for genetic screens.

Strain	Relevant Genotype	Reference
RS1606	MC4100, rho^{WT}, P_{RM}-*racR*-t_{rac}-*lacZYA*, $rpoC^{ts}$, tet^{R}	This study
RS1714	MC4100 *gal EP3*, rho^{Y80C}	This study
RS1729	MC4100 rho^{Y80C}, P_{RM}-*racR*-t_{rac}-*lacZYA*	This study
RS1758	MC4100, rho^{Y80C}, P_{RM}-*racR*-t_{rac}-*lacZYA*, $rpoC^{ts}$, tet^{R}	This study
RS1428	MC4100, rho^{WT}; P_{RM}-*racR*-t_{rac}-*lacZYA*	(*35*)
DJ354	MG1655, *rpoC* 120 btu::Tn10 *(*ter^{R}*, ts)*	From Din Jin
Plasmids		
pRS513	pBAD18M-$rpoC^{WT}$ with C-terminal HMK-His tag, amp^{R}	(*83*)
pRS1973	pBAD18M–$rpoC^{C70A}$, amp^{R}	This study
pRS1974	pBAD18M–$rpoC^{C70H}$, amp^{R}	This study
pRS1975	pBAD18M–$rpoC^{C72A}$, amp^{R}	This study
pRS1976	pBAD18M–$rpoC^{C72H}$, amp^{R}	This study
pRS1977	pBAD18M–$rpoC^{C85A}$, amp^{R}	This study
pRS1978	pBAD18M–$rpoC^{C85H}$, amp^{R}	This study
pRS1979	pBAD18M–$rpoC^{C88A}$, amp^{R}	This study
pRS1980	pBAD18M–$rpoC^{C88H}$, amp^{R}	This study
pRS1981	pBAD18M–$rpoC^{C70A,C72A}$, amp^{R}	This study
pRS1982	pBAD18M–$rpoC^{C70A,C72A,C88A}$, amp^{R}	This study
pRS1983	pBAD18M–$rpoC^{C70A,C72A,C85A,C88A}$, amp^{R}	This study
pRS1984	pBAD18M–$rpoC^{E86K}$, amp^{R}	This study
pRS1985	pBAD18M–$rpoC^{G82D}$, amp^{R}	This study
pRS1986	pBAD18M–$rpoC^{Y75N}$, amp^{R}	This study

Captions for Movies S1 and S2

Movie S1.

Overview of the engagement complex. Rendering of individual images was done with PyMOL. The movie was compiled with Windows Movie Maker.

Movie S2.

Model for EC-dependent, ρ-mediated termination. The movie shows stages of an EC-dependent, ρ-mediated transcription termination pathway as deduced from our cryoEM analysis. Coordinates were morphed using PyMOL. Rendering of individual images was done with PyMOL. The movie was compiled with Windows Movie Maker.